RSC Advances

ROYAL SOCIETY OF CHEMISTRY

www.rsc.org/advances

Journal Name

RSCPublishing

ARTICLE

Reduced graphene oxide anchored with zinc oxide nanoparticles with enhanced photocatalytic activity and gas sensing property

Jianjiang He[a], Chunge Niu[b], Chao Yang[a], Jide Wang[a], Xintai Su[a]*,

Cite this: DOI: 10.1039/x0xx00000x

Received 00th January 2012,
Accepted 00th January 2012

DOI: 10.1039/x0xx00000x

www.rsc.org/

Reduced graphene oxide (rGO)-zinc oxide (ZnO) composites were synthesized by a two-step hydrolysis-calcination method, using GO and $Zn(Ac)_2$ as precursors. The structure and morphology of as-prepared samples were characterized by thermogravimetric analysis, X-ray diffraction, Fourier transforms infrared spectroscopy, transmission electron microscopy and field emission scanning electron microscopy. It was shown that the well-dispersed ZnO nanoparticles (NPs) were deposited on rGO homogeneously. So far as ZnO NPs with different diameters were synthesized in the varied samples, the ZnO NPs with an average diameter of around 10 nm which was obtained at the heating temperature of 300 ^oC for 4 h exhibited higher photocatalytic activity than others. The relatively low amount of rGO-ZnO composites (5 mg) demonstrated enhanced photocatalytic activity to decompose methyl orange (MO, 40 mg L^{-1}) and methylene blue (MB, 10 mg L^{-1}) under low-power ultraviolet light. Furthermore, rGO-ZnO composites exhibited high sensitivity, and the response can be achieved 50.09 to 1000 ppm acetone. In addition, the ultraviolet light-induced photocatalytic mechanism as well as gas sensing mechanism was also discussed. Both rGO and crystallinity played important roles in improving photocatalytic activity and gas sensing property.

1. Introduction

Recently, environmental problems such as air and water pollution have provided the impetus for sustained fundamental and applied research in the area of environmental remediation. As a promising candidate for use in waste water purification and toxic gas detecting, ZnO shows its great potential in the applications in gas sensor and photocatalysts [1-3]. Besides the wide band gap, the major limitation to achieve high photocatalytic efficiency and gas sensing response in ZnO structure system is the quick recombination of charge carriers. Over the past decades, the composite method have been proved to be an effective route to improve the performances of ZnO photocatalysts and gas sensors, such as semiconductor-noble metal composites [4, 5], semiconductor-semiconductor composites [6, 7], semiconductor-carbon materials composites [8-10]and so on.

In recent years, rGO flourishes in composite materials due to its conductivity, large surface area, absorption capability and superior electron mobility which will benefit for the photocatalytic and gas sensitive performances [11-14]. The ultrathin flexible rGO layers not only can provide a support for anchoring well-dispersed nanoparticles (NPs) and work as a highly conductive matrix for enabling good contact between them [15, 16], but also can effectively prevent the volume expansion/contraction and aggregation of NPs during photocatalytic and gas sensing measuring process [17-19]. Meanwhile, the anchoring of NPs on rGO can effectively reduce the degree of restacking of graphene sheets and consequently keep their high active surface area and, to some extent, increase the photocatalytic and gas sensing performance of graphene-based material [20, 21]. It is well known that the NPs have advantages, such as of larger relative surface areas, less particle momentum, higher mobility, and better suspension stability over their bulk counterparts due to the large contact area between the NPs and the reactant molecules. Therefore, it is believed that the composite of flexible and electrically conductive graphene anchored with nanostructured ZnO particles can efficiently utilize the combinative merits of nanosized ZnO and graphene and obtain photocatalysts and gas sensors with superior performance. Although many graphene-ZnO composites were successfully synthesized [8, 13-15, 22], seldom report devote to thermal fabrication of rGO-ZnO composites at different temperature conditions.

Herein, we report a mild and simple strategy to synthesize ZnO NPs anchored on rGO as an advanced semiconducting material with enhanced photocatalytic and gas-sensing performance. The ZnO NPs obtained are spherical with an average diameter of around 10-20 nm in size and homogeneously anchor on graphene sheets as spacers to keep the neighboring sheets separated. These rGO-ZnO composites display superior

Journal Name RSCPublishing

ARTICLE

Fig. 1 Schematic presentation of the fabrication of rGO-ZnO.

synergistic effect for the decolorization of methyl orange (MO) and methylene blue (MB) dyes when exposed to ultraviolet (UV) irradiation. Meanwhile, the composites exhibit a high response for acetone and ethanol. The rGO which has excellent adsorption capacity and electronic transfer capability may responsible for both the enhanced photocatalytic and gas sensing performance of ZnO. This work, highlighting the importance of the anchoring of NPs on graphene sheets for maximum utilization of active ZnO NPs and rGO, thus have shown that the as-prepared rGO-ZnO composites may be used as high-performance photocatalysts and gas sensors.

2. Experimental

2.1 Fabrication of rGO-ZnO composites

A typical synthesis process is as follows: water-soluble $Zn(Ac)_2$ solution was prepared by mixing 1.0975 g of $Zn(Ac)_2$ (5 mM), 0.7010 g of hexamethylenetetramine (5 mM) and 0.1471 g of sodium citrate (0.5 mM) in 100 mL of deionized water to form solution A. GO (0.1 g) was ultrasonicated in 100 mL of deionized water to form a GO solution (solution B). The two solutions were mixed and stirred at room temperature for 0.5 h, then ultrasonicated and heated at 90 ^oC for 5 h. After then, the products were washed by deionized water and ethanol and dried at 80 ^oC overnight to obtain the dried GO-zinc precursor. The series products were obtained by the further calcinated GO-zinc precursor at 260 ^oC for 1 h (rGO-ZnO-1), 260 ^oC for 4 h (rGO-ZnO-2), 300 ^oC for 1 h (rGO-ZnO-3), 300 ^oC for 4 h (rGO-ZnO-4) and 350 ^oC for 4 h (rGO-ZnO-5), respectively (Figure 1). The above products were calcined with a heating rate of 1 ^oC min^{-1} under an environmental atmosphere. The pure zinc precursor was fabricated by the above steps without GO, and the pure ZnO was obtained by the further calcinated at 300 ^oC for 4 h with a heating rate of 1 ^oC min^{-1}. GO was synthesized from graphite purchased from Aladdin, using the Staudenmaier method and developed by other authors [23].

2.2 Characteristics

Crystallographic information was investigated by X-ray diffraction (XRD) patterns, which were measured on a Brucker D8 GADDS diffractometer using Cu Kα radiation. Thermogravimetric analysis (TGA) was performed under air flow from room temperature to 800 ^oC using a Perkin-Elmer Pyris 1 TGA apparatus. Fourier transform infrared (FTIR) spectroscopy over the range of 4000-400 cm^{-1} was recorded on a NEXUS 470 spectrometer, using KBr pellets. The morphology was characterized by transmission electron microscopy (TEM) images using a Hitachi H-600 and field emission scanning electron microscopy (FESEM) images using a Hitachi S-4800. Brunauer-Emmett-Teller (BET) specific surface areas were determined from the nitrogen adsorption apparatus (JW-BK, China) at 77 K.

2.3 Photocatalytic Experiments

Typically, 5 mg of photocatalysts (ZnO or rGO-ZnO composites) were added to 50 mL of aqueous solution of the methyl orange (MO) dyes (40 mg L^{-1}). Prior to the irradiation, the suspensions were magnetically stirred in the dark for 75 min. Afterward, the photoreaction vessel was exposed to the UV irradiation (100 W mercury lamp, 365-366 nm) under room temperature. The light intensity at the position of quartz tube is 12.7 mW cm^{-2}. The suspension was analyzed by recording variations of the absorption peak maximum in the UV-visible spectra of MO using a UV-visible spectrophotometer (Shimadzu) UV-2550. The batch experiments of the degradation of MB were similar with this.

2.4 Gas-sensing Test

Gas-sensing test was carried out by a WS-30A gas response instrument. The fabrication process of rGO-ZnO composites sensors was as follows: as-prepared rGO-ZnO composites were mixed with ethanol and then coated onto an Al_2O_3 tube, on which two platinum wires have been installed at each end for connecting the coated materials. The operating temperatures were controlled by adjusting the heating power, using a Pt wire placed through the Al_2O_3. The response was calculated as the ratio R_a/R_g for the reducing gases. R_a is the electrical resistance

of the particles exposed to the air and R_g is the resistance measured when the particles are exposed to the target gases.

3. Results and discussion

Fig. 2 shows the powder XRD patterns of the GO and a series of rGO-ZnO composites. The diffraction pattern of GO has a peak centered at 2θ = 12.9°, corresponding to the (001) reflection (Fig. 2a). The XRD patterns of rGO-ZnO composites can be well indexed to a tetragonal cell with a = b = 3.24982 Å and c = 5.20661 Å, in good agreement with the standard data (JCPDS No. 36-1451). The diffraction patterns of composites do not show any change in comparison with those of pure ZnO (Fig. 2g). However, the reflection of rGO is not observed in the XRD patterns of rGO-ZnO composites because the regular stack of rGO sheets were homogeneously dispersed and coated with ZnO NPs [24]. The extremely weak intensity of ZnO in Fig. 2b-d can be ascribed to its poor crystallinity or low content or both. More importantly, as the heat treatment temperature increases, the XRD peaks of rGO-ZnO composites gradually become strong, indicating that the crystallinity increases, meanwhile the corresponding crystallite size gradually becomes large [22]. Compared with rGO-ZnO-4, pure ZnO which suffered same heat treatment shows increased crystallinity. This suggests that the thermal stability of ZnO is increased after composited with rGO. From Fig. 2, the full width at half maximum (FWHM) values from the (100) reflection of rGO-ZnO-2, rGO-ZnO-3, rGO-ZnO-4, rGO-ZnO-5 and ZnO are calculated as 1.109, 0.977, 0.899, 0.528 and 0.805, respectively. And the (100) reflection of rGO-ZnO-1 is not obvious that we cannot obtain the FWHM value. We propose that the order of increasing crystallinity is rGO-ZnO-5 > ZnO > rGO-ZnO-4 > rGO-ZnO-3 > rGO-ZnO-2 > rGO-ZnO-1.

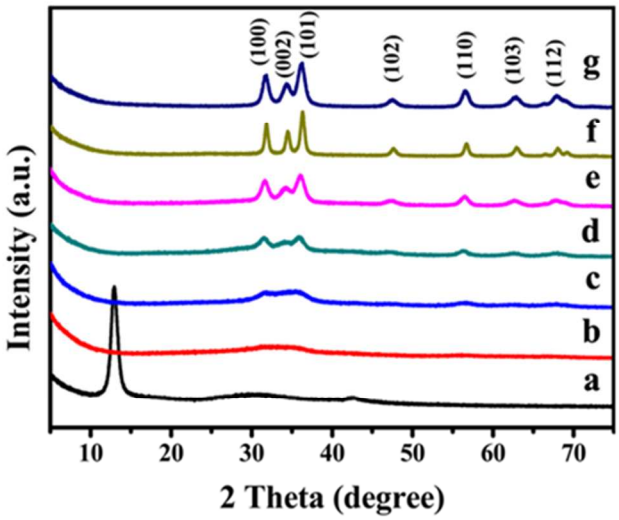

Fig. 2 XRD patterns of GO and rGO-ZnO composites synthesized with different calcination temperature (a) GO, (b) rGO-ZnO-1, (c) rGO-ZnO-2, (d) rGO-ZnO-3, (e) rGO-ZnO-4, (f) rGO-ZnO-5 and (g) pure ZnO.

The GO and rGO-ZnO composites were characterized by FTIR spectrum and TGA. In the FTIR spectrum of the GO (Fig. 3a), the strong and broad absorption located on 3409 cm^{-1} can be assigned to the stretching vibrations of O-H. The broad absorption peaks at around 1053 and 1623 cm^{-1} are attributed to the characteristic stretching vibration of C-O and C=O. The bending vibration of O-H displays characteristic absorptions at 1390 cm^{-1}. All of these peaks were extremely weakened in the FTIR spectrum of rGO-ZnO-4 and rGO-ZnO-5. Meanwhile, the absorption peak at 1559 cm^{-1} might be attributed to the stretching vibration of C=C. All of these results indicate the transformation from GO to rGO. Furthermore, the absorption peak at 439 cm^{-1} for the rGO-ZnO composites can be assigned to the stretching vibration of Zn-O, which is blue-shifted from 410 cm^{-1} of Zn-O in the bulk ZnO. TGA was used to determine the thermal stability. As shown in Fig. 3b, GO shows two significant weight losses at about 220 and 650 °C are consistent with pyrolysis of the labile oxygen-containing functional groups and decomposition of carbon framework, respectively. The TGA curves (Fig. 3b) of the rGO-ZnO composites show weight loss from room temperature to 200 °C, which may be due to the desorption of surface bound water. The weight loss from 200 to 700 °C could be attributed to the removal of oxygen-containing groups and the decomposition of carbon framework from the composites. On the basis of the TGA analysis, the rGO-ZnO composites show a good stability until 400 °C.

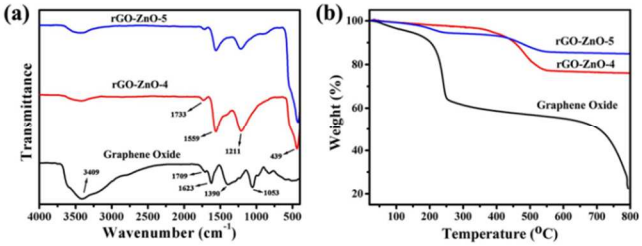

Fig. 3 (a) Fourier transform infrared (FTIR) spectra and (b) Thermogravimetric analysis (TGA) curves of GO and rGO-ZnO composites.

To further characterize the morphology of the rGO-ZnO composites, TEM observations were conducted. In Fig. 4a, the GO sheets are entirely covered by flower-like zinc precursor. The ultrathin film of zinc precursor will benefit for the fabrication of small sized ZnO NPs. As can be seen from Fig. 4g, the zinc precursor without GO is still flower-like film. From Fig. 4b-f, it can be observed that flower-like zinc precursors on the GO sheets are gradually collapse as the heating temperature increased and the ZnO NPs progressively grown up. It can be seen from Fig. 4b, the flower-like zinc precursor became collapse under the temperature of 260 °C. As shown in Fig. 4c, the ZnO begin to form accompanied by flower-like zinc precursor collapses as the heating time prolonged. From Fig. 4d, we can observed that flower-like zinc precursors were completely collapse with increasing the heating temperature up to 300 °C, and the diameters of ZnO NPs are approximately 8

nm. The diameters of ZnO NPs grow up to about 10 nm when keep on heating for another 3 h (Fig. 4e). As continued increasing the heating temperature up to 350 ^{o}C, the ZnO NPs which anchored on the rGO will keep on growing to reach the diameters of 20 nm (Fig. 4f). From Fig. 4, we can observe that the heating temperature is crucial to the formation and growth of phase. The particle size will grow up with either increasing heating temperature or prolonging heating time. Compared with rGO-ZnO-4, the pure ZnO NPs without rGO which undergo the same heating treatment were easy to agglomeration and tend to have a big particle size (15-20 nm) (Fig. 4h).

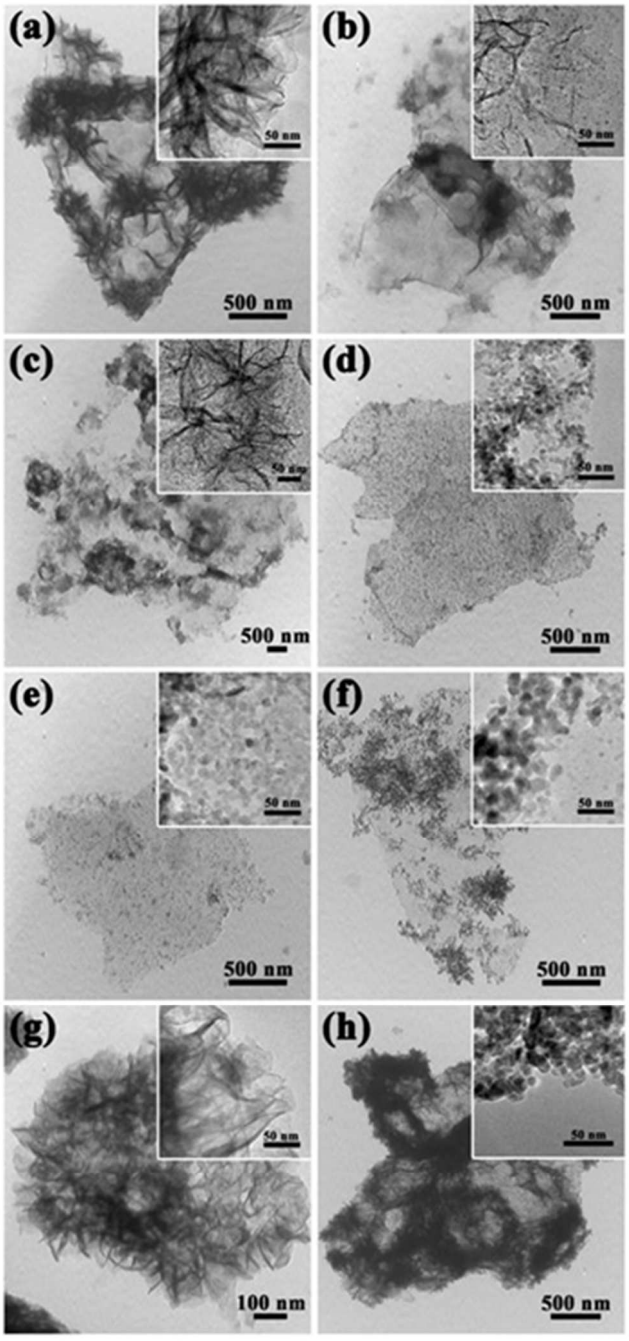

Fig. 4 TEM images of different products (a) GO-Zinc precursor, (b) rGO-ZnO-1, (c) rGO-ZnO-2, (d) rGO-ZnO-3, (e) rGO-ZnO-4, (f) rGO-ZnO-5, (g) Zinc precursor, (h) ZnO.

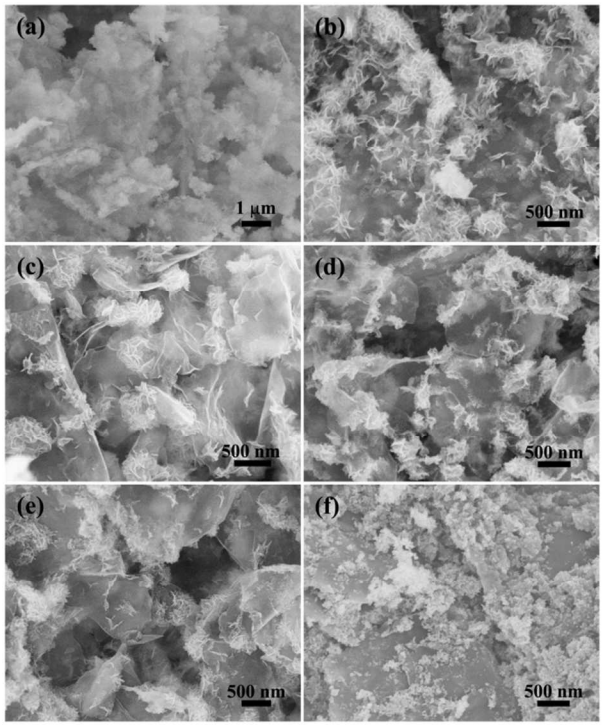

Fig. 5 FESEM images of different products (a) GO-Zinc precursor, (b) rGO-ZnO-1, (c) rGO-ZnO-2, (d) rGO-ZnO-3, (e) rGO-ZnO-4, (f) rGO-ZnO-5.

The layer structures are also observed by FESEM. Consistent with the above SEM analysis, the zinc precursors and ZnO NPs are homogeneously covered on the rGO sheets (Fig. 5a-f). From another point of view, the morphology of the products evolved from flower-like structures to NPs with the temperature increased. Meanwhile, the rGO sheets stacked together, which can be identified with the collapse of the flower structure. Specifically, Fig. 5f shows that the rGO-ZnO-5 composite displays markedly aggregation behaviour. The specific surface area calculated by BET method also ascertains the aggregation phenomenon (Table S1).

In order to better investigate the performance of rGO-ZnO composites, the UV-visible absorption spectra are introduced. Fig. 6a shows the UV-visible absorption spectra of rGO-ZnO composites and ZnO. And there are subtle changes in their optical absorption peaks. According to the reported equation [25], measured direct band-gaps of rGO-ZnO-1, rGO-ZnO-2, rGO-ZnO-3, rGO-ZnO-4, rGO-ZnO-5, and ZnO were estimated to be 2.71, 2.88, 3.12, 3.14, 3.20, and 3.03 eV, respectively. All of the products present a narrow band gap than ZnO in the literature report [26]. The low band gaps of ZnO and rGO-ZnO composites may be attributed to low crystallinity and impurity which result in the formation of impurity energy level between valence band and conduction band [27, 28]. From Fig. 6b we can observe the phenomenon that the band gaps of rGO-ZnO composites are increased as the calcined temperature increased.

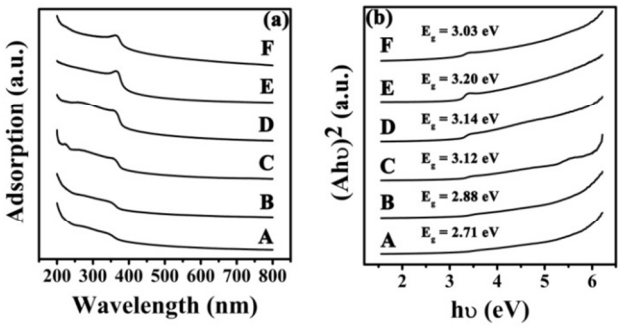

Fig. 6 (a) The UV-visible absorption spectra and (b) Plots of (Ah□)2 versus photon energy (h□) of (A) rGO-ZnO-1, (B) rGO-ZnO-2, (C) rGO-ZnO-3, (D) rGO-ZnO-4, (E) rGO-ZnO-5 and (F) ZnO.

The order of band gap is rGO-ZnO-5 > rGO-ZnO-4 > rGO-ZnO-3 > ZnO > rGO-ZnO-2 > rGO-ZnO-1. From the order of crystallinity and band gaps of rGO-ZnO composites, we propose that the crystallinity is crucial to band gap energy [29]. Furthermore, rGO also influence the band gap energy because of the conjugation bond between rGO and ZnO NPs [30]. Based on the above analysis, the photocatalytic and gas sensing performance of rGO-ZnO and ZnO were explored.

The photocatalytic performance of rGO-ZnO composites and ZnO was evaluated by examining the degradation of methyl orange (MO) as a representative pollutant under irradiation from a 100 W high-pressure mercury lamp (12.7 mW cm^{-2}). Prior to irradiation, the photocatalytic reaction system was magnetically stirred in the dark for 75 min to reach the adsorption/desorption equilibrium of MO on the surface of the photocatalysts. Fig. 7a-b shows the UV-visible absorption spectrum of the aqueous solution of MO (initial concentration, 40 mg L^{-1}, 50 mL) with 5 mg of ZnO or rGO-ZnO-4 for various durations. The characteristic absorption of MO at 463 nm decreases rapidly with extension of the exposure time, and almost disappears after about 150 min for rGO-ZnO-4. The color change sequence in the MO solution during this process is shown in the inset of Fig. 7c, from which it is clear that the intense orange color of the initial solution gradually disappears with increasingly longer exposure times. To demonstrate the synergy-induced enhancement of the photocatalytic efficiency of rGO-ZnO composites, contrastive experiment was performed using pure ZnO particles as photocatalyst for the photodegradation of MO. The results of the MO degradation using a series of photocatalysts are summarized in Fig. 7c. There was hardly any degradation of MO solution under irradiation without any photocatalyst (blank). The rGO-ZnO-4 shows the most superior photocatalytic performance among rGO-ZnO composites which may be attributed to both crystallinity and synergistic effect with rGO. The high crystallinity is essential to enhance the generation of electron-hole pairs and can reduce the number of defects to prevent electron-hole pairs from recombination [31, 32]. However, the improvement of crystallinity is often accompanied by increase in particle size and stacks the layered rGO, which is not conductive to the formation of large amounts of active sites.

The photocatalytic mechanism of metal oxide semiconductor is not investigated distinctly [33]. Some groups maintaining that the photocatalytic process is referred to as a catalyzed photoreaction. The initial photoexcitation occurs in an adsorbate molecule which then interacts with the ground state catalyst substrate [21]. While other groups maintain that the process is a sensitized photoreaction, in which the initial photoexcitation takes place in the catalyst substrate and the photoexcited catalyst then transfers an electron or energy into a ground state molecule [14, 34]. In a catalyzed photoreaction, an electronic transmission is forbidden by the separation between molecule and catalyst substrate. It is expected to show less adsorption capacity, and will be unlikely to cause photochemical conversions which involve such a transition. From Fig. 7c, it can be seen that rGO-ZnO-5 still demonstrates excellent photocatalytic performance without any adsorption. On the basis of experimental and theoretical results, we propose that the rGO-ZnO-based photoreaction is a sensitized photoreaction rather than a catalyzed photoreaction.

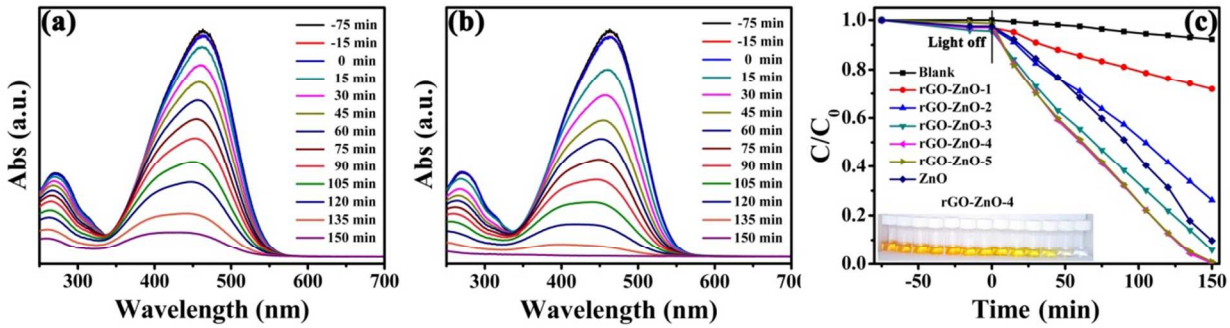

Fig. 7 UV-visible absorption spectra of MO solution during the photodegradation by different photocatalysts of (a) ZnO and (b) rGO-ZnO-4. And (c) the degradation of MO in the presence of various ZnO and rGO-ZnO composites.

Journal Name RSCPublishing

ARTICLE

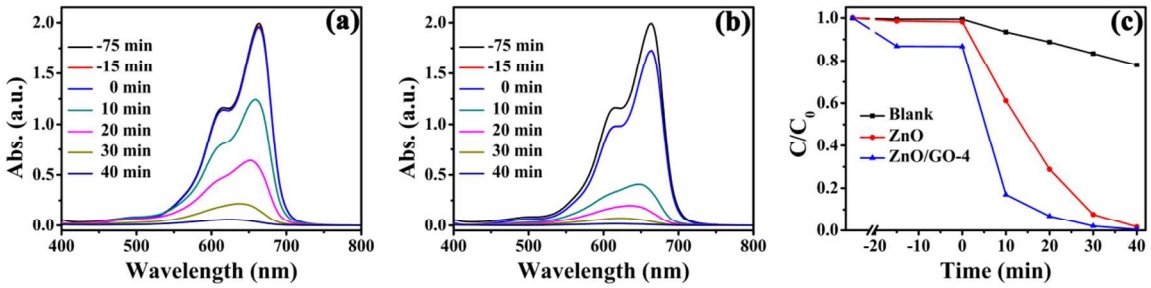

Fig. 8 UV-vis absorption spectra of MB solution during the photodegradation (a) ZnO, (b)rGO-ZnO-4, and the degradation of MB in the presence of various photocatalysts.

For further study on photocatalytic mechanism, we also did the batch experiment of photodegradation methylene blue (MB). Fig. 8a-b shows the UV-visible absorption spectrum of the aqueous solution of MB (initial concentration, 10 mg L^{-1}, 50 mL) with 5 mg of ZnO or rGO-ZnO-4 for various durations. About 83% of MB was removed in 10 minutes after illumination in presence of rGO-ZnO. By contrast, there are only 39% and 7% of MB were removed in presence of ZnO NPs and blank, respectively. From Fig. 8c, it is can be observed that there is sharply adsorption (about 13%) on the surface of rGO-ZnO-4 in the solution of MB. And the rGO-ZnO-4 composite showed enhanced photocatalytic performance compared with ZnO NPs and blank. Several mechanisms have been proposed to account for the photodegradation of organics with photocatalysts [1, 33, 35]. We believe that this excellent performance of rGO-ZnO-4 can be attributed to two aspects. The reaction mechanisms on the surface of photocatalysts appear to be very close related to both the surface-adsorbed molecules and transfer of charge carriers [36]. On the one hand, MB molecules can be transferred from the solution to the surface of ZnO and adsorbed with offset face-to-face orientation by π-π conjugation between MB and aromatic regions of rGO, and therefore, adsorption of dyes increases compared to that of the bare ZnO [12, 37]. The MB molecules adsorbed on the surface of photocatalysts are more easily decomposed than those in the solution [34]. On the other hand, the heterojunctions between rGO and ZnO provide an internal electric field that facilitates separation of the electron-hole pairs and induces faster carrier migration [38].

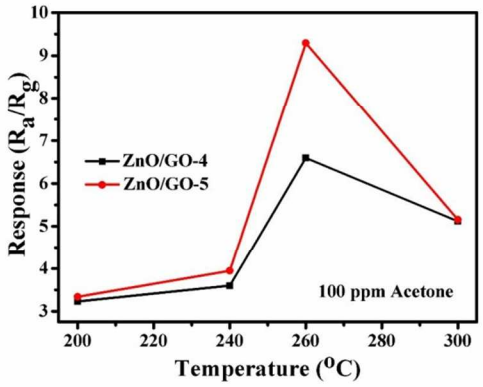

Fig. 9 The real time response for rGO-ZnO based gas sensors to heat-voltage at an acetone concentration of 100 ppm.

Similarly, the adsorption capacity and electronic transfer capability are essential for the gas sensing performance of ZnO. To prove graphene can further improve the sensing performance of ZnO, we investigated the sensing properties of rGO-ZnO composites to inorganic compound. Here, we choose acetone as the studied compound which is due to their important applications in our daily life and industry. It is well known that the response of a semiconductor gas sensor is highly influenced by its operating temperature. Firstly, we determined a suitable heating voltage for sensors to achieve the high response through varying the heating voltage. Fig. 9 shows the response to heat-voltage at an acetone concentration of 100 ppm. The results show that the rGO-ZnO-based sensors had the highest response under the temperature of 260 °C.

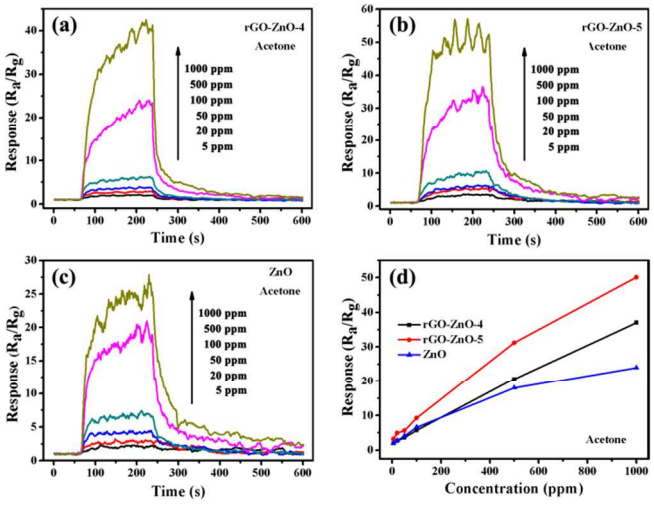

Fig. 10 Response to concentration of acetone for the sensors: (a-c) real time response curves and (d) the average response.

At the optimized operating temperature of 260 °C, Fig. 10(a-c) shows the real time gas sensing response of rGO-ZnO-4, rGO-ZnO-5 and ZnO. It is clearly showed that the sensors are sensitive to acetone. Even at a very low gas concentration (5 ppm), the sensor can achieve strong and stable signals compared to the baseline. The gas concentration was then increased, and other cycles were recorded at different vapour concentrations of 20, 50, 100, 500, and 1000 ppm, respectively. As can be seen, gas response increases abruptly upon the injection of gases, and then decreases rapidly to their initial state after the test gases are released. Compared with pure ZnO, the rGO-ZnO composites show a better stability which can be observed from the smooth real time response curves and shorter recovery time. Fig. 10d shows the average response to concentration of acetone for sensors. We can observe that rGO anchored with ZnO show better gas sensing performance compared with pure ZnO NPs. Specifically, the response of rGO-ZnO-5 based sensor toward acetone at the concentration of 1000 ppm is 50.09, which is higher than 37.00 for rGO-ZnO-4 and 23.93 for ZnO NPs. It may be due to the high crystallinity, high adsorption capacity and conductivity of rGO-ZnO-5. For one thing, as same as photocatalytic activity, the high crystallinity is also enhance gas sensing performance and there are also many O_2 molecules adsorbed on the surface of rGO-ZnO composites via π-π conjugation which can improve the gas sensitivity. For another, applied for gas sensors, the crystallinity of rGO-ZnO composites rather than particle size is the crucial parameter for the gas sensitivity.

The response of rGO-ZnO composites-based gas sensors toward ethanol was also investigated. As shown in Fig. S1, all the sensors demonstrate a good response to ethanol which means that the sensors have no selectivity toward acetone and ethanol. And importantly, the rGO anchored with ZnO show better gas sensing performance than the pure ZnO NPs.

The rGO shows the most important influence both on the performance of photocatalytic and gas sensitivity. It was because the layered structure will benefit for adsorption and fast carrier migration (Fig. 11).

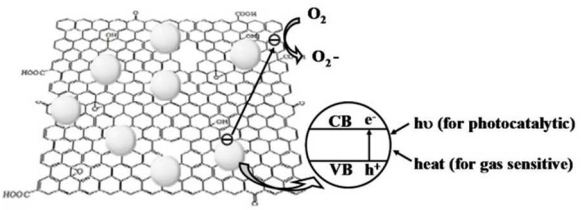

Fig. 11 The mechanical illustration of high photocatalytic activity and enhanced gas sensing performance for rGO-ZnO composites.

4. Conclusion

The rGO-ZnO composites have been prepared through a hydrolysis-calcination method with enhanced photocatalytic activity and gas sensing performance. The adsorption capacity and high conductivity of rGO are supposed to be responsible for excellent performance. The calcined rGO-ZnO composites show different trends in the performance of photocatalytic activity and gas sensitivity which can be attributed to crystallinity and particle size. This easily approach to rGO-ZnO composites provides new ways to achieve enhanced photocatalytic and gas sensing performance.

Acknowledgments

This work was supported by National Natural Science Foundation of China (51174174) and Excellent Talents of Xinjiang Province (2013721015)..

Notes and references

[a] Ministry Key Laboratory of Oil and Gas Fine Chemicals, College of Chemistry and Chemical Engineering, Xinjiang University, Urumqi 830046, China.
[b] Petrochemical Research Institute, Karamay Petrochemical Company, Karamay 834700, China.
* Corresponding author. Tel. & fax: +86 991 8581018. E-mail address: suxintai827@163.com (X. Su).

1 H. Tong, S.X. Ouyang, Y.P. Bi, N. Umezawa, M. Oshikiri, J.H. Ye, *Adv. Mater.*, 2012, **24**, 229.
2 Y. Zhang, J.Q. Xu, Q. Xiang, H. Li, Q.Y. Pan, P.C. Xu, *J. Phys. Chem. C*, 2009, **113**, 3430-3435.
3 T.J. Sun, J.S. Qiu, C.H. Liang, *J. Phys. Chem. C*, 2008, **112**, 715.
4 P. Li, Z. Wei, T. Wu, Q. Peng, Y.D. Li, *J. Am. Chem. Soc.*, 2011, **113**, 5660.
5 X.H. Liu, J. Zhang, L.W. Wang, T.L. Yang, X.Z. Guo, S.H. Wu, S.R. Wang, J. Mater. Chem., 2011, **21**, 349.
6 C. Wang, J.C. Zhao, X.M. Wang, B.X. Mai, G.Y. Sheng, P.A. Peng, J.M. Fu, *Appl. Catal., B*, 2002, **39**, 269.
7 D.L. Liao, C.A. Badour, B.Q. Liao, *J. Photochem. Photobiol., A*, 2008, **194**, 11.
8 O. Akhavan, *Carbon*, 2011, **49**, 11.
9 O. Akhavan, *ACS nano*, 2010, **4**, 4174.
10 G. Williams, P.V. Kamat, *Langmuir*, 2009, **25**, 13869.

11 T.G. Xu, L.W. Zhang, H.Y. Cheng, Y.F. Zhu, *Appl. Catal., B*, 2011, **101**, 382.
12 Q.J. Xiang, J.G. Yu, M. Jaroniec, *Chem. Soc. Rev.*, 2012, **41**, 782.
13 J.L. Wu, X.P. Shen, L. Jiang, K. Wang, K.M. Chen, *Appl. Surf. Sci.*, 2010, **256**, 2826.
14 Y. Yang, L. Ren, C. Zhang, S. Huang, T. Liu, *ACS Appl. Mater. Interfaces*, 2011, **3**, 2779.
15 Z.Y. Zhan, L.X. Zheng, Y.Z. Pan, G.Z. Sun, L. Li, *J. Mater. Chem.*, 2012, **22**, 2589.
16 Y.J. Mai, D. Zhang, Y.Q. Qiao, C.D. Gu, X.L. Wang, J. Tu, *J. Power Sources*, 2012, **216**, 201.
17 K.F. Zhou, Y.H. Zhu, X.L. Yang, X. Jiang, C.Z. Li, *New J. Chem.*, 2011, **35**, 353.
18 Y.M. Sun, X.L. Hu, W. Luo, Y.H. Huang, *ACS nano*, 2011, **5**, 7100.
19 S. Deng, V. Tjoa, H.M. Fan, H.R. Tan, D.C. Sayle, M. Olivo, S. Mhaisalkar, J. Wei, C.H. Sow, *J. Am. Chem. Soc.*, 2012, **134**, 4905.
20 S.M. Cui, S. Mao, G.H. Lu, J.H. Chen, *J. Phys. Chem. Lett.*, 2013, **4**, 2441.
21 H. Seema, K.C. Kemp, V. Chandra, K.S. Kim, *Nanotechnology*, 2012, **23**, 355705.
22 H.X. Chang, Z.H. Sun, K.Y.-F. Ho, X.M. Tao, F. Yan, W.M. Kwok, Z.J. Zheng, *Nanoscale*, 2011, **3**, 258.
23 W. Li, J.P. Yang, Z.X. Wu, J.X. Wang, B. Li, S.S. Feng, Y.H. Deng, F. Zhang, D.Y. Zhao, *J. Am. Chem. Soc.*, 2012, **134**, 11864.
24 S. Yang, X. Feng, S. Ivanovici and K. Muellen, *Angew. Chem. Int. Ed.*, 2010, **49**, 8408.
25 T. Yu, B. Lim, Y.N. Xia, *Angew. Chem. Int. Ed.*, 2010, **49**, 4484.
26 A. Tsukazaki, A. Ohtomo, T. Onuma, M. Ohtani, T. Makino, M. Sumiya, K. Ohtani, S.F. Chichibu, S. Fuke, Y. Segawa, *Nat. Mater.*, 2005, **4**, 42.
27 D.Y. Wang, H.C. Lin, C.C. Yen, *Thin Solid Films*, 2006, **515**, 1047.
28 A. Luque, A. Martí, *Phys. Rev. Lett.*, 1997, **78**, 5014.
29 J. Aarik, H. Mändar, M. Kirm, L. Pung, *Thin Solid Films*, 2004, **466**, 41.
30 M. Kertesz, C.H. Choi, S.J. Yang, *Chem. Rev.*, 2005, **105**, 3448.
31 Z.W. Zhang, Y.M. Zhou, Y.W. Zhang, S.J. Zhou, J.J. Shi, J. Kong, S.C. Zhang, *Dalton Trans.*, 2013, **42**, 5004.
32 V. Puddu, H. Choi, D.D. Dionysiou, G.L. Puma, *Appl. Catal., B*, 2010, **94**, 211.
33 A.L. Linsebigler, G. Lu, J.T. Yates Jr, *Chem. Rev.*, 1995, **95**, 735.
34 H. Zhang, X. Lv, Y. Li, Y. Wang, J. Li, *ACS nano*, 2009, **4**, 380.
35 D.F. Ollis, E. Pelizzetti, N. Serpone, *Environ. Sci. Technol.*, 1991, **25**, 1522.
36 Y. Yu, J.C. Yu, C.Y. Chan, Y.K. Che, J.C. Zhao, L. Ding, W.K. Ge, P.K. Wong, *Appl. Catal., B*, 2005, **61**, 1.
37 J.H. Liu, Z.C. Wang, L.W. Liu, W. Chen, *Phys. Chem. Chem. Phys.*, 2011, **13**, 13216.
38 C.H. Kim, B.H. Kim, K.S. Yang, *Carbon*, 2012, **50**, 2472.

